2021 Collegiate Wind Competition Technical Report

NORTHERN ARIZONA UNIVERSITY

May 23, 2021

Team Member	Team and Title	Contact Information
	MECHANICAL TEAM	
Barry Benson	Machinist	bjb448@nau.edu
Tore Cadman	CAD Consultant	tsc97@nau.edu
Bryce Conner	Project Lead (Primary Author)	bsc225@nau.edu
Joseph Conroy	DAQ Developer	jc3552@nau.edu
Stanley Kennedy	Capstone Liaison	ask98@nau.edu
Aaron Zeek	Aerodynamicist	acz34@nau.edu
	ELECTRICAL TEAM	
Benjamin Allen	Software Developer	bra92@nau.edu
Noah Bell	Electrical Lead	nsb85@nau.edu
Evan Kramer	Budget Liaison	edk37@nau.edu
Nolan McNeil	Hardware Developer	npm53@nau.edu
Aidan Nash	Technical Lead	aen73@nau.edu
	ADVISORS	
David Willy	Principal Investigator	David.Willy@nau.edu
Venkata Yaramasu	Electrical Consultant	Venkata.Yaramasu@nau.edu
Sarah Oman	Senior Design Coordinator	Sarah.Oman@nau.edu
David Trevas	Senior Design Instructor	David.Trevas@nau.edu

CONTENTS

I. Executive Summary

The following report is the summation of Northern Arizona University's efforts in the 2021 Collegiate Wind Competition (CWC) held by the United States Department of Energy (DOE). The CWC encourages students at a variety of wind energy institutions to design, fabricate, and test a micro-scale wind turbine within the boundaries prescribed by the DOE in the 2021 CWC rules and regulations (RR) [1]. Upon completion of the project, students were to attend the competition to test the developed turbines in a public and competitive environment. However, due to the unpredictable circumstances brought on by the global pandemic, this stage of the competition has been forgone. The DOE as well as advisers at the National Renewable Energy Laboratory (NREL) have encouraged independent testing of the turbines appropriate to each university's capacity. NAU has made efforts to develop a data acquisition (DAQ) system that has been utilized to provide informative data to the state and efficiency of the manufactured turbine.

The group's design goal is to produce a safe and efficient turbine. This is done through the optimization of all components relevant for testing, as discussed in Section II. After the identification of the team's objective, following sections are assigned to each critical sub-system. Within these individual sections the team's design, analysis, and static experimentation of said sub-systems are discussed. This begins with the blade design, where the team constructed and employed a MATLAB algorithm along with the open-source program Q-Blade to converge on an aerodynamically and structurally appropriate design. Next the pitch system is introduced. The driven pitch system was chosen to be a hybrid linear bearing connected to mounted bearings through Heim joints. The driving system of the pitch was selected as a stepper motor pushing a gear train of miter, spur, and rack gears. This design is complimented by static experimentation that lead the team to utilize a specific pitch orientation. The braking and yawing systems are then discussed. The brake uses a linear actuator to clamp a steel disk onto a rubber backing in the nacelle in tandem with the stalling of the blades to reduce torque production, resulting in high factors of safety (FOS) without the concern of sheering the blades. The yawing is enacted by a passive yawing fin and complimented by a nacelle-tower connection methodology that utilizes two steel bearings to pinch the nacelle into place once the designed retainer locks the mechanism. The remaining components of the turbine (nacelle, hub, shaft, and base-plate) follow these trends in a more condensed fashion, discussing the key engineering requirements of each part and how said requirements were met.

In the final sections of the report, the electrical subsystem, design overview, and dynamic testing results are explored. The electrical analysis does not only depict the layout chosen to transmit mechanical power to electric power, but also the considerations that were made to aid in the turbine's optimum performance through an extensive control algorithm in charge of monitoring and/or adjusting the status of the pitch, brake, load connection, and emergency push button. The mechanical and electrical components are then combined and visualized. The remainder of the overview section will then discuss the turbine's conformity to constraints established in the RR in terms of safety and installation. Lastly, the efforts depicted in these section are dynamically tested in the prescribed environments to confirm the validity of each sub-system on an assembly level.

II. Design Objective

The NAU 2021 CWC team's (AeroAXE) objective is to design, fabricate, and test a micro-scale wind turbine as per the specifications of the 2021 RR that will operate efficiency and safely among the other submissions from the prestigious wind energy institutions throughout the nation competing in this year's CWC. This will be achieved by addressing all categories listed in Table A-2 of the RR [1]. Although the global pandemic has rendered the rubric listed for the testing of the turbine in Table A-3 of the RR no longer applicable, the group will remain resilient and persist in this individualistic environment and design with these rigorous tests acting as the driving factors. The team will emphasize the brake safety and the development of an appropriate power curve, but all other sections including start-up, rated control, and overall durability will be addressed with the full intent of obtaining as many (theoretical) points as possible.

A. Summary of Regulations

The DOE puts forth many regulations in regard to the fabrication of the micro-scale wind turbine. These regulations are not only present for accurate comparisons of the different university's turbines, but to also ensure the safety of the students and faculty involved in the testing of said turbines. Table I summarizes these regulations.

TABLE I
Turbine Design Constraints

Description	Target
Aerodynamic	
Cut-in wind speed	2.5 - 5 m/s
Operating wind speed	5 - 11 m/s
Rated wind speed	11 m/s
Testing wind speed	$\leq$13 m/s
Theoretical wind speed	$\leq$22 m/s
Dimensional	
Rotor volume	45x45x45 cm
Rotor centerline height from base	60 (±3 cm)
Base-plate diameter	$<$15 cm
Base-plate thickness	$<$16.1 mm
Reference diameter for fasteners	4.5 in
Mounting bolt diameter	10 mm
Electrical	
DC output voltage	$<$48 V
Tower resistance to ground	$<$100 kΩ
Turbine side capacitance	$<$10 J
Turbine side battery capacitance	0 J
Load side AC supply voltage	120 V

III. Aerodynamics and Blade Design

The aerodynamics of the turbine were the first considerations made in the early design stages of the project. Although vertical axis wind turbines (VAWTs) show promise in reduced wake production and flexibility in erratic flow fields, the group's design quickly converged to a horizontal axis wind turbine (HAWT) in consideration of the typical inefficiencies associated with VAWTs. Utilizing the mathematically intensive process that is described in *Wind Energy Explained* [2], the group compiled a MATLAB algorithm that produced an ideal blade shape with tip loss and wake considerations. Blades that showed promising C_p vs λ curves were then replicated in Q-Blade to produce more comprehensive analyses. It was determined that the inclusion of a pitching system would greatly enhance the group's design. For the trade-off of mechanical complexity the turbine would still remain competitively efficient in terms of both start-up and operating conditions. Finally, a sturdy connection methodology that is able to resist the maximum centrifugal forces of the micro-scale wind turbine was developed through finite element analyses (FEA).

A. MATLAB BEM Algorithm

The blade element momentum (BEM) theory suggests that by breaking a blade into segments and examining the aerodynamic phenomena on a differential level, an optimum blade shape and its respective efficiency can be calculated. The algorithm's required inputs are as follows: blade radius (R), design tip speed ratio (λ), airfoil specifications at each segment, rated wind speed (U), and number of blades (B).

$$C_p = f(R, \lambda, c, C_D, C_L, U, B) \tag{1}$$

Where c, C_D, and C_L are the airfoil chord length, drag coefficient, and lift coefficient, respectively. The computationally challenging aspect of the algorithm is the calculation of lift and drag forces.

These forces are functions of the angle of attack (α) and the Reynolds number (RE). By identifying the α at which the maximum lift to drag ratio (C_L/C_D) occurs for different values of RE, the optimum twist can be found for each blade segment when considering the rated values for U and λ.

Therefore, in order to properly operate the algorithm needed an array of airfoil data at varying RE values. XFOIL is an interactive program for analyzing airfoils embedded within Q-Blade which produces these data sets. Starting at a RE value of 3000, RE values up to 150,000 were simulated with increments of 1000. These values enveloped all possible conditions according to the group's early calculations. This in tandem with a small increment produced a comprehensive data base that allowed the group to catch any aerodynamic consequences due to subtle geometry changes. Figure 1 displays the data used to locate the optimum α, at which point separate data sets containing individual C_L and C_D values were retrieved from directories called upon by the program.

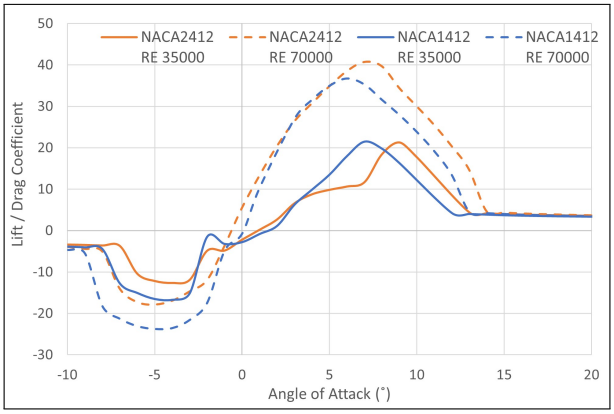

Fig. 1. C_L/C_D vs α

When considering the number of airfoils the group was interested in investigating along with the amount of data present in each file, the group stored over 80 data sets with each individual file consuming roughly 175 KB of storage. This resulted in extensive calculation times taking as long as two hours to converge. After adjustments to the algorithm's logic and convergence factor, run times as low as 30 minutes were experienced without any sacrifices in accuracy. After utilizing the algorithm many times, a three-bladed rotor with a design λ of 4 that incorporates the NACA2412 airfoil at its root and transitions to the NACA1412 for the mid-span and tip was selected. This combination resulted in a maximum aerodynamic efficiency of 43.1%, as supported by Figure 3 (seen in the following section comparing the algorithm results to a blade of the same shape using Q-Blade). This blade shape was selected not only for the high efficiency displayed, but also for the tendencies it exhibited prior to the operating λ, which indicated strong performance (C_p=25%) as early as $\lambda = 3$.

B. Q-Blade Analysis

Although the information produced by the team's MATLAB algorithm is vital to the production of the blade, extensive analysis needs to be performed outside the confines of the algorithm to understand the comprehensive characteristics of the blade. Torque production at lower wind speeds, inefficiencies at non-operating conditions, the benefits of pitching, and evaluation of runaway scenarios are all considerations that will prove beneficial to the team's design.

The first consideration is torque production at low winds speeds. As per the RR, the group is interested in power production at wind speeds as low as 2.5 m/s. In reflection of this, the group investigated the blade's performance at 3 m/s. According to static experimentation performed on the rotary system of the turbine, torque values should reach up to 0.02 N·m to produce any rotational movement. This is above the threshold exhibited by the MATLAB blade (Iteration I). Even after exaggerating the chord length at the root of the blade to increase solidity, therefore torque production, the inflated torque values the group attained were negligible at lower λ values. That is until the inclusion of pitching, which raised the torque differential of each blade from 0.4 N·mm to 5 N·mm when pitched 40°, as seen in Figure 2. Utilizing a pitching system, the rotor would ideally produce 0.0198 N·m at 3 m/s. In light of the drastic torque increase displayed by the magnified solidity, the geometry changes to the blade were implemented (iteration II) into the team's final design and were utilized in tandem with a pitching system to approach optimal start-up aerodynamics.

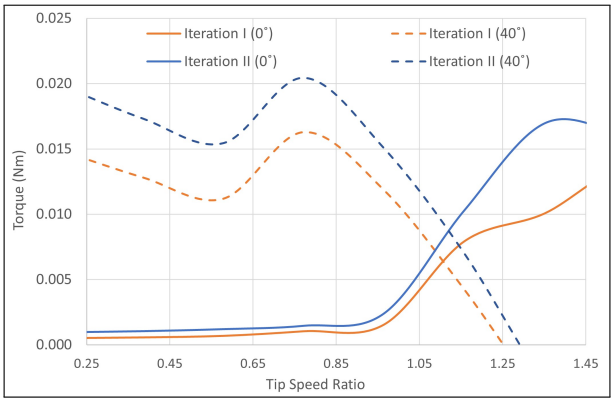

Fig. 2. Cut-in Torque Comparison at 3 m/s

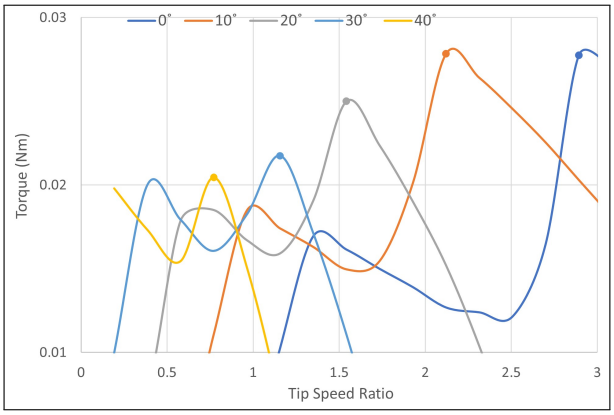

Fig. 4. Torque at 3 m/s with Varying Pitch (Iteration II)

Changes in geometry which aim to aid the conditions of certain operating scenarios often result in a decline in performance in other areas. However, blade iteration II displayed aerodynamic properties on par and even superior to iteration I (Figure 3). Apart from the design changes that will arise from a new ideal λ of 3.5 and the inefficiencies that appear after a λ of 4, the amended blade boasts a higher maximum efficiency of 45.1% along with more promising trends at lower rotational velocities.

The inclusion of an active pitching system solves one of the largest problems seen in lift machines by increasing torque production in low wind regimes, but introduces a considerable amount of complexity to the control algorithm. The complications arise from the relationship of torque with wind and rotational speed as exhibited in Figure 4. Until streamlines disconnect, increasing pitch will result in the maximum torque occurring at a lower λ at the cost of said torque's magnitude. The control algorithm would ideally start at a pitch of 40° and then adjust until operation conditions for that wind speed are achieved. However, the variables that are required to find optimum pitch vary frequently in flow fields of this size. This encouraged the group to make estimations of ideal conditions utilizing the turbine's power production, discussed further in Section VIII.

Before confirming the final design, it is pertinent to examine conditions in which the generator is disconnected from the load and is free to accelerate to the runaway λ value which will produce excessive centrifugal forces. The identification of this value relies on the convergence of the BEM iterator at rotational speeds that surpass rated λ. Since BEM iterators can have issues with stability

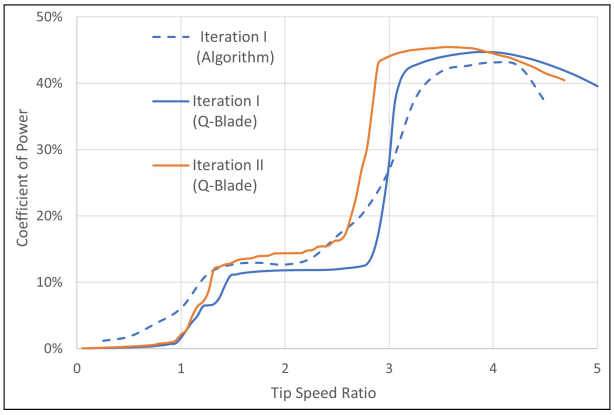

Fig. 3. C_p vs λ at 11 m/s

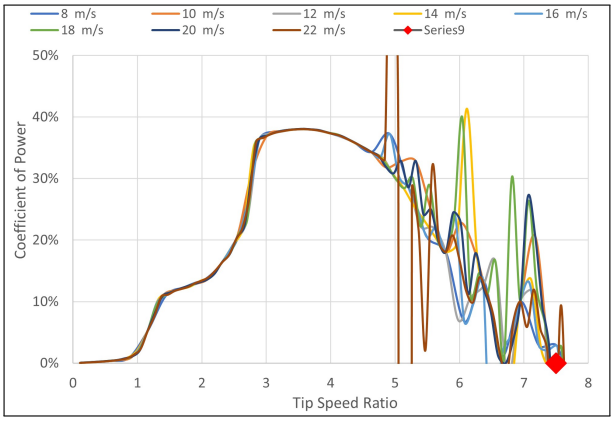

Fig. 5. Runaway λ Values for Different Wind Speeds

in this region, the group used several different C_p vs λ curves to approximate this value, as seen in Figure 5. It is apparent that most wind speeds have a runaway λ range that straddles 7.5. This results in rpm values up to 8100 when considering the existing geometry.

The final data that needed to be extracted from Q-Blade is the power curve and its respective annual energy production. Assuming operating conditions that would result in maximum power output for each wind speed, the turbine has a rated power output of 60 W. Using a variety of Rayleigh distributions, the annual energy production was derived assuming average wind speeds of the same range as seen in Figure 6.

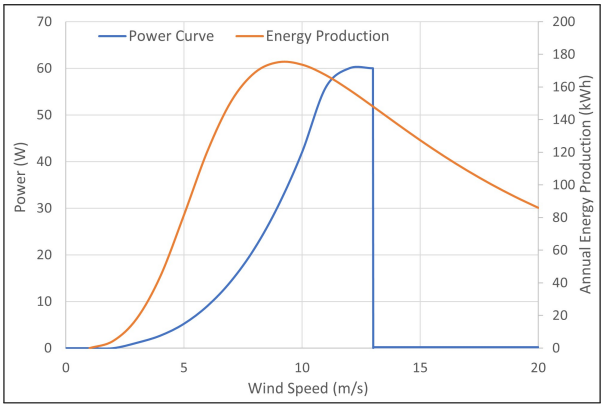

Fig. 6. Power and Energy Production vs Wind Speed

C. Structural Analysis

Any object placed within a flow field and expected to remain fastened to a single point will experience thrust forces. In regard to turbines, the calculation of this force is a function of the field's dynamic pressure and the axial induction factor (a).

$$T = \frac{1}{2}\rho A U^2 \left[4a\left(1-a\right)\right] \tag{2}$$

In parked conditions, the second half of the equation involving the axial induction factor becomes irrelevant and the maximum rotor thrust can be evaluated as 11.4 N. However, dynamic conditions will alter the inputs to this equation. Inclusion of an ideal axial induction factor (1/3) and the new swept area will result in forces on the order of 31.1 N.

The calculation of thrust production on the rotor is important for the safety of many sub-systems, but the largest stress sources stem from the centrifugal forces. This design will require stresses lower than the tensile strength of the final material to avoid catastrophic mechanical failure. The group predicts that with the existing blade geometry forces up to 6.2 kN could be experienced. This results in stresses up to 18.4 MPa. However, concentrations due to rapid changes in the blade's cross section still pose a threat beyond this. In order to confirm that the selected blade geometry can be supported by the available materials, an FEA analysis was performed implementing the maximum values of thrust and rotational velocity. Figure 7 shows that a majority of the mid-span experiences stresses on the order of what was predicted.

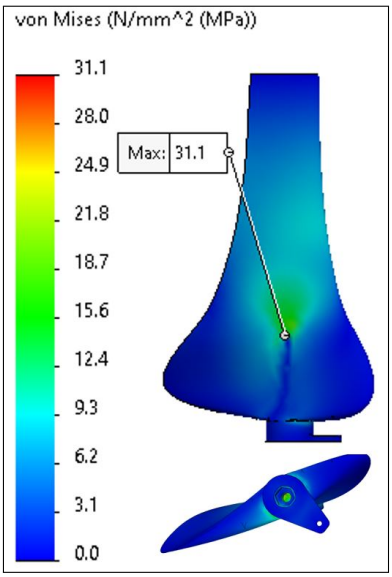

Fig. 7. Blade FEA Analysis

However, stress concentrations with magnitudes up to 31.1 MPa are found at the bolt connection. Referencing experimental data, the tensile strength of PLA is on the order of 36.5 MPa [3]. Therefore, the FOS is 1.17. As this phenomenon only occurs when the load disconnects, which will trigger the control systems to park the turbine, the FOS should prove sufficient considering the minimal exposure the turbine will have to these forces.

The group performed a strength test to confirm the above FOS. Seen in Figure 8, the blade was fastened upside down from a ladder suspended

wooden 2”x4”. Weights in the form of 80 lbs concrete bags were added to loading apparatus. For the safety of the on-site personnel, after every 80 lb bag was added, 80 lbs of lifting weights were added and removed in increments to confirm the blade was capable of suspending another bag. Due to spacial restrictions and the lack of proper facilities, only 480 lb (2.13 kN) was added before safety concerns arose. Although this did not reach the maximum forces predicted at 22 m/s for runaway, the achieved loading is 6.3 times the magnitude predicted in optimum operation and 0.98 times the maximum test runaway (13 m/s).

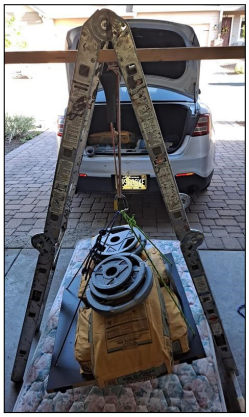

Fig. 8. Blade Loading

D. Finalized Blade Shape

The final design employs the shape that was developed through MATLAB and improved by Q-Blade iterations. The design also needed a connection methodology to the mounted bearings and Heim joints utilized in the driven pitching system, further discussed in Section IV. For the bearing connection, a 60 mm M6 bolt threads into carefully dimensioned plastic using a high torque drill in tandem with the presence of a hex bolt coupler secured with epoxy. The Heim joint connection is on a flange that extends from the base of the blade with a 30° offset from operating for optimum pitch range. In consideration of this offset, the group included a cut on the flange to signal the pitch position. All of these features are present in Figure 9. Table II also lists information regarding the chord length and twist at each segment along the blade. The fabricated blade is also shown in further detail within Section IX.

IV. Pitching

As derived in the previous section, the aerodynamic freedom that is introduced by the implementation of a pitching system encouraged the team to follow this design path. The system has the driven and

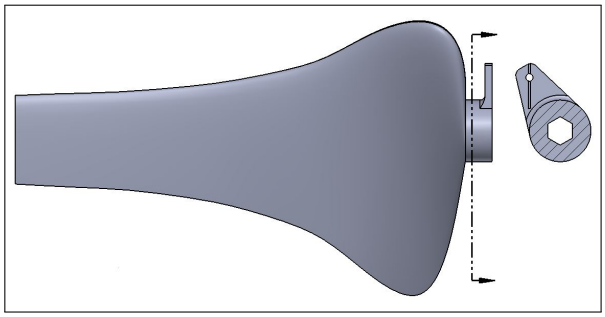

Fig. 9. Final Blade with Connections

TABLE II
Blade Dimensions

Radius mm	Airfoil	Chord mm	Twist °
0	Circular	25	N/A
11	Circular	25	N/A
30	NACA 2412	130	31.6
50	NACA 2412	105	22.5
70	NACA 2412	70	16.2
90	NACA 1412	60	13.4
110	NACA 1412	50	10.3
130	NACA 1412	44	8.0
150	NACA 1412	40	6.3
170	NACA 1412	38	4.9
190	NACA 1412	36	3.8

driving components. A modified swash-plate is used to connect these two systems. Heim joints and mounted bearings were then used to fasten the blades to the pitching system and hub. The inclusion of these kinematic devices allowed for multiple degrees of freedom to prevent binding of the driven system and reduced friction faced by the driving system, which consists of a stepper motor and gear train that allows for the linear movement along the shaft.

A. Driven Pitch System

The system was inspired by the previous 2020 NAU CWC team who attempted to utilize two linear actuators symmetric about the shaft to push a swash plate and alter the pitch by turning physical adapters between the hub and blades [4]. Upon reverse engineering, the group found several areas to improve upon.

Firstly, the previous team’s shaft was a thin steel shaft, in contrast to the thick aluminum shaft fabricated for this year’s competition. The clearance diameter of the previous swash plate

was too small for the newer shaft. However, swash plates of larger diameter showed a drastic increase in price. This reality, coupled with the fact that swash plates feature a 2nd degree of freedom required for cyclic pitching that is essential when operating helicopters but useless in micro-scale turbine application, the group decided to forgo an outsourced part and design a linear hybrid bearing that would grip the shaft allowing for extra support of the rotating axis, minimal resistive torque, and a more cost effective product. The final iteration of this part can be seen in Figure 10. The hybrid linear bearing was 3D-printed in four segments prior to the insertion of individual ball bearings and then sealed with epoxy in post processing.

The group also sought to include mechanisms to reduce the innate friction of the system. Rather than mounting the rotating component of the blade directly to the hub and relying on the power of the driving system to force rotation, the group used mounted bearings to connect the hub and blades. The use of Heim joints was then imitated and connected via 3D-printed couplers, as they proved efficient in the prevention of binding between the fastened parts.

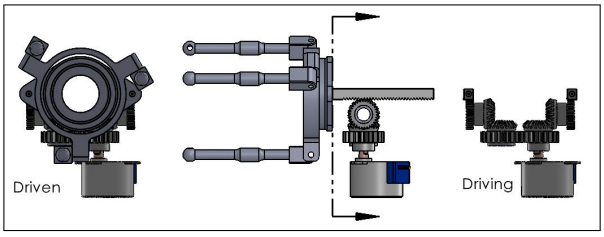

Fig. 10. Pitching System

B. Driving Pitch System

In regard to the driving pitching system, the group considered the use of linear actuators, but the lack of precise control available for actuators led the group to utilize a stepper motor to give the system more agency over pitch and therefore experienced aerodynamics. After some debate on the most spatially efficient way to translate the rotational movement to the desired linear movement, a gearing system that utilizes miter, spur, and rack gears was implemented. This methodology allowed for a compact design and served as the foundation of the upper nacelle blueprints. The fabricated system is also displayed in Section IX.

C. Pitch Sub-System Testing

A majority of the thrust force derived in Section III will be supported by the shaft or translated into the displacement of the blades. This displacement will be a phenomenon that the driving servo of the pitching mechanism will need to either support or counteract. Figure 11 shows the testing apparatus that was used to find the point at which the stepper motor failed to pitch forward. Varying sizes of Jenga blocks (12g-170g) were added to a 3D-printed platform that was inserted within the vertically oriented upper nacelle. The apparatus was powered by a 6V input and controlled by two push buttons to pitch forward and backward. In the process, the group found the implemented stepper motor failed to push loads above 3.3 N (0.74 lb). To account for the minimal holding torque derived through this experiment, the team chose a particular pitching orientation to compliment this constraint. The pitching mechanism will push when seeking to increase torque and pull when seeking to lower torque at low and high wind regimes, respectively. The idea of over pitching the blades to decrease torque production in strenuous flow conditions is discussed further in Section V. This methodology creates an environment where the driving system will not face extensive thrust forces when seeking

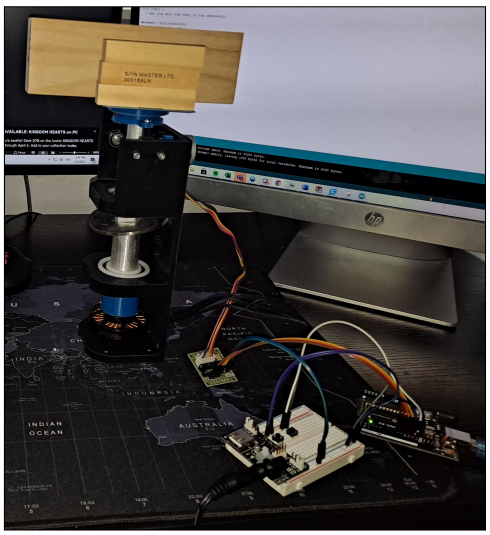

Fig. 11. Pitching Test Apparatus

to move forward and will only need to overcome the innate friction of the system while also utilizing said thrust forces when attempting to stall.

V. Braking

The braking system is a floating disk which uses a linear actuator to apply a clamping force to pinch a steel disk against a rubber brake pad and backing. In tandem with this stopping force, the inclusion of the pitching system allows for the natural decline of the aerodynamic forces acting upon the blades, greatly reducing the potential of shearing off the rotor due to the rapid change in rotational kinematics. The capabilities of these mechanisms are mathematically analyzed and statically exposed to the relevant forces. Due to the simplicity of the sub system, in place of a CAD drawing, the fabrication is seen in Section IX.

A. Floating Disk Brake

A standard floating disk brake system that applies a clamping force with an actuator is the primary means of parking the turbine. The group originally planned to use two actuators symmetric about the shaft. However, further investigation proved this method to be excessive. The finalized design features a rubber brake pad which pushes the disk against a rubber nacelle backing in place to prevent the excessive heating of the 3D-printed plastic used in the nacelle. The inclusion of this backing was inspired by test results of previous NAU CWC teams where parts were warped due to excess friction. With the 50 N axial force produced by a single PQ12-P Actuonix actuator, the minimum estimated friction factor between dry rubber and steel at 0.6 [5], and the acting distance of the actuator, the braking torque available to the system is on the order of 3.45 N·m. When comparing this to the expected maximum torque values at 22 m/s shown in Figure 12, the brake disk has a FOS of 2.3. The magnitude is increased further by the inclusion of the turbine's pitching capabilities.

B. Pitching to Stall

Another aspect of pitching was briefly discussed in Section IV, which is the ability to pitch the blades to stall. This gradually decreases torque production. If the blades are in operating conditions at 22 m/s, the turbine has the potential of producing up to 1.49 N·m of torque. After pitching forward 15°, this value occurs at a much lower λ with a magnitude of 0.44 N·m. Although continuing to increase pitch will result in a lowered maximum torque and ease of braking, the group has only allotted for 10° of control. This design was encouraged by the limited pitch range derived from the confined linear space available while taking into account the larger range required for desirable start-up characteristics as depicted previously in Figure 4. This lowers the maximum required torque production of the brake disk to 0.65 N·m, raising the FOS to 5.3. In addition to the lowered torque, the induced reduction in rotational velocity will lower the chances of a blade shearing off due to the sudden rotational deceleration.

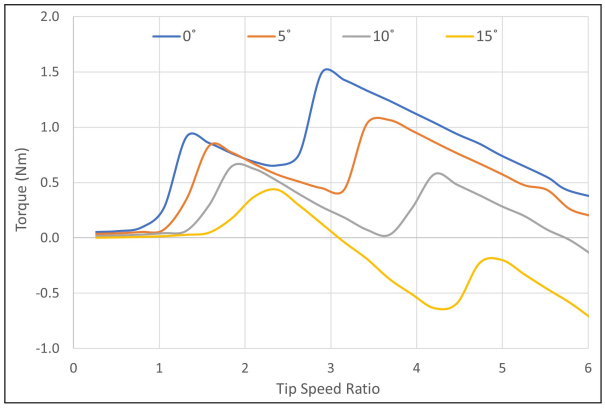

Fig. 12. Torques Reduced by Stall at 22 m/s

C. Brake Static Performance

The testing of these sub-systems prior to assembly will help ensure the validity of the braking process. Figure 13 is representative of the apparatus fabricated for testing the holding torque of the brake disk when clamped by the fully extended linear actuator powered by 6 V. The actuator is controlled by two push buttons that extend and retract the shaft. The weights are the same Jenga blocks implemented in the pitching tests. The upper nacelle is locked in place using duct tape. The lever arm designed for this experiment in tandem with the cardboard volume serving as a load capacity exert a natural torque of 0.21 N·m. After adding 26.9 N, the disk began to slip. The holding torque achieved was 2.64 N·m. This value is slightly lower

than the predicted values based on the spec sheets of the equipment, but still provides FOS of 1.8 and 4.1 when considering braking from operating and stalled conditions.

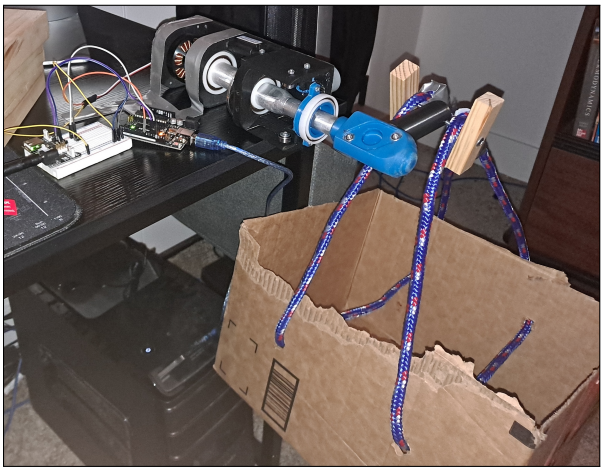

Fig. 13. Braking Test Apparatus

In regard to pitching, the group has seen superb results in static experimentation. The group confirmed that the stall was enough to prevent rotation up to 40 mph (17.9 m/s). Despite the strong performance, Figure 12 would predict similar results even at operating pitch conditions. Further confirmation of the aerodynamic response when stalling from high rotational velocity is required to confirm the mechanism's true effectiveness.

VI. Yawing

Yawing refers to the active or passive system utilized to ensure the orthogonal relationship between the rotor plane of the HAWT and the fluid direction. In micro-scale turbines, active yaw systems are cost inappropriate as well as unnecessary. Due to the loss of efficiency associated with down-wind rotors (one strategy for passive yawing) and the 45 cm range permitted to the team, the yawing fin design route was followed. Through trial and error, different iterations of the group's fin geometry was analyzed at different offsets from alignment and wind speeds until appropriate forces were achieved. To induce the rotation of the turbine, the nacelle's connection to the tower needed to employ mechanisms that permit said rotation. The structural integrity of said connection was then tested.

A. Passive Yaw Fin

The use of a passive yawing fin is common practice in small scale wind turbines. A surface area parallel to the flow field and extended from the axis of rotation (the tower) will result in a yawing system that employs the dynamic pressure innately available in the fluid. Mathematical modeling of this phenomenon requires considerations of the fin's geometry and position. Through augmentation of the equation for dynamic pressure, the team performed further analysis by means of Equation 3.

$$T_{yaw} = \frac{1}{2}\rho U^2 x_c(\theta) \int_0^{L(\theta)} z(x)\, dx \qquad (3)$$

Where the torque production of the yaw is a function of the fluid conditions and exposed area of the fin set by the angle at which the rotor and flow are offset from alignment (θ). In the case that the fin is not a uniform plate, the distance from the axis of rotation (x) will alter the height (z), which when integrated along the length of the exposed fin (L) will return the area. Finally, the force's magnitude is then scaled by the acting distance, identified by the exposed area's center of mass (x_c). In order to apply Equation 3, a preexisting geometry is required. Upon the third iteration of the fin, seen in Figure 14, sufficient torque production was seen to counteract the resistivity of the nacelle-tower connection along with the torque on the rotor due to induced thrust forces previously derived. The fin is split into two segments along the mid-span to allow for 3D-printing despite the size of the part. The wings are placed at an 8° offset to improve the performance of the fin at lower values of θ. The fin's wings also take the profile of the NACA0009 airfoil, as inspired by Pennsylvania State University's 2019 CWC design [6]. Drafts extend from the nacelle-fin connection point. These two aspects were included

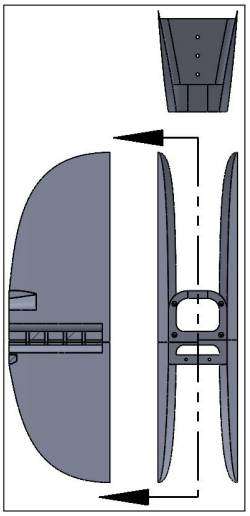

Fig. 14. Yawing Fin

in an attempt to reduce the formation of eddies behind the turbine. The fabricated yaw is depicted in Section IX.

B. Nacelle-Tower Connection

The inclusion of a yawing fin creates the need for a nacelle connection to the tower that permits rotation. A standard two-stage bearing train was implemented that feeds through an opening in the bottom of the lower nacelle. The tower diameter has a slight step down to secure the inner lip of the bottom bearing. The nacelle (not shown in Figure 15) is then inserted, followed by another bearing which clamps the nacelle using the outer lips of both bearings. In initial blueprints, the final steps were the inclusion of a retaining ring to secure the assembly and a slip ring placed atop the tower to allow for the rotation of the nacelle without the entanglement of wiring.

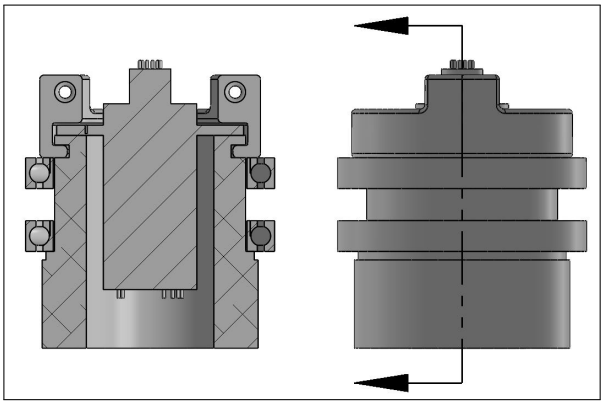

Fig. 15. Nacelle-Tower Connection

Through fabrication, the group found two issues with this methodology. The first is a tolerance issue that arose between the outsourced bearings, retaining ring, and machined tower. The available space resulted in excess tilt that reduced the efficiency of the turbine. The second issue was the minimal fastening methodologies available to the slip ring. The team addressed these aforementioned problems by developing a two-part retainer that would fill the entirety of the tower's indent, clamp down the slip ring, and align the top support bearing with the tower. By introducing a 3D-printed part to the sub-assembly, the team was capable of iterating on dimensions until an optimized system was fabricated without the consequences of purchasing inappropriate components or redoing cost intensive machining.

C. Stress Investigations

The component likely to fail under excessive shear stress within the sub-system is the *straddle* of the lower nacelle that is clamped by the bearings. An FEA was performed based on the induced torque from the thrust on the rotor. Figure 16 displays the results and indicate a FOS of 11.4.

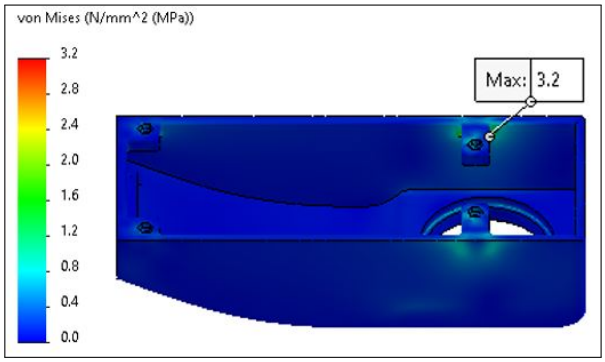

Fig. 16. Nacelle-Tower Connection FEA

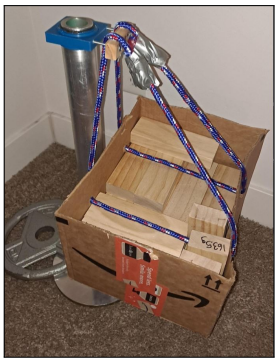

Fig. 17. Connection Testing

From there, static testing of the part exhibited the capability of the turbine to not only withstand the expected forces during operation but also confirmed the absence of any binding within the mechanism. Jenga blocks were added to a loading apparatus as seen in Figure 17. After each addition, the apparatus was rotated 360° four times to confirm that movement would not induce mechanical failure or binding. The group added 69.4 N before experiencing issues with the spatial loading capacity. This weight resulted in a torque value of 4.51 N·m. Although the group was unable to test until failure, the value reached is above that of the expected maximum 3.81 N·m calculated through thrust and geometric considerations.

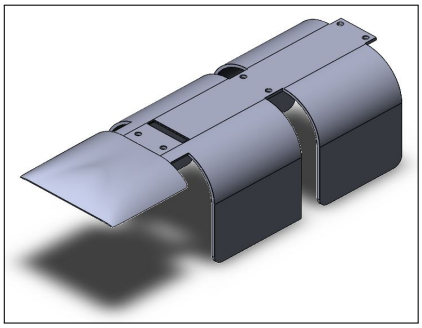

Fig. 18. Cover

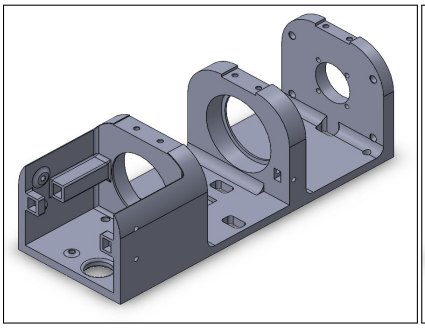

Fig. 19. Upper Nacelle

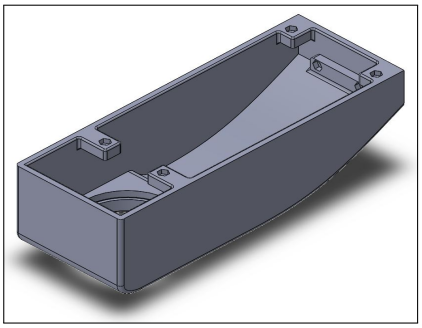

Fig. 20. Lower Nacelle

VII. Other Mechanical Components

Within the past year, the team has spent nearly 2600 hours researching, designing, and reporting on the contents of the turbine. The entirety of the story cannot be comprehensively expressed within twenty pages. The following section will report on components that received no less mathematical or engineering analysis than other sub-systems but do not highlight the more distinctive aspects of the team's design. All of these parts' printed/machined models can be seen in Section IX.

A. Nacelle

The nacelle can be dissected into three sections, the upper and lower nacelles along with the cover. The upper nacelle houses the brake disk, linear actuator, driving pitch system, generator, and support bearing. It also must connect to the lower nacelle, cover, and fin. The part needed to be carefully toleranced considering the amount of sub-systems that rely on the dimensions of the component. The part was 3D-printed four times before all aspects were appropriately sized with changes to the last iteration on the order of 0.15 mm.

The lower nacelle was previously shown in an FEA (Section VI). Apart from withstanding sheer stress, the lower nacelle needs to provide space for the slip ring, wiring, retainer, electrical headers, driver board, and stepper motor. Four connection points for the upper nacelle and two for the fin are also present. These connections utilize an epoxy secured hex nut but also thread into a portion of the plastic itself.

The cover is derived from the shape of the upper nacelle. The cover should not interfere with any of the components while making a semi-flush surface to prevent the formation of eddies within the sections of the nacelle.

B. Hub

Since the hub consumes space that is valuable to the translation of wind energy to mechanical power, it should be as minimal as possible without sacrificing structural stability. The hub provides a center clearance for the bolt head protruding from the mounted bearing and adjacent clearances for the hex couplers that secure said bearing to the hub. An adhesive FOS of 2.4 is obtained by maximizing the surface area of the epoxy secured coupler at the cost of no plastic threading. However, when considering runaway at the maximum theoretical wind speed, the hub has an insufficient FOS (0.54). Since RPM and voltage are directly related, this issue can be solved by the inclusion of an over voltage protection event that is discussed further in Section VIII. This raises the hub's FOS to 3.11.

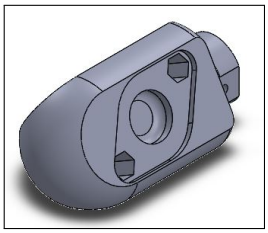

Fig. 21. Hub

C. Shaft

A plastic shaft was considered in the early stages of the project, but the weight of the rotor acting on the shaft caused bending, leading to an array of inefficiencies. The shaft includes several step downs to allow for insertion into the hub, brake disk, and generator coupler. A maximum stress of 1.4 MPa was identified through the use of previously derived

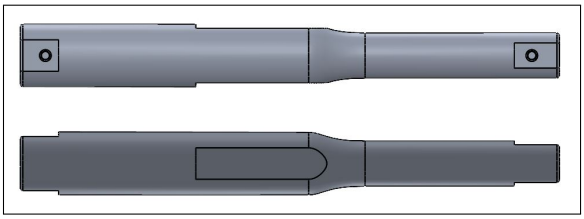

Fig. 22. Aluminum Shaft

values (Section III) in an FEA. When considering the tensile strength of aluminum, the FOS is 183.6 [7]. This exaggerated value is a result of initial dimensions assuming a plastic shaft. This drove the sizing of other components in the initial design phases, resulting in shaft geometry that had to be retained even after switching materials.

D. Base-plate

The aluminum tower was welded to an aluminum base-plate. Although this methodology results in an excessively large FOS of 24.5. The utilized manufacturing process was cost appropriate and simple for experienced welders. This part is seen manufactured in Section IX.

VIII. Electrical Interface

The fabrication of the electrical systems to transfer the mechanical energy produced by the turbine into usable electrical power is the final sub-system. This topology is depicted in Figure 23. This begins with the use of a 110 kV MAD generator selected for its strong performance at low rotational velocities. The FUS 45-0045B six diode rectifier was then utilized to convert the turbine's output from an AC to DC voltage. A DROK LTC1781 DC/DC step up converter is employed to reach a rated 30 V. Prior to this step up, voltage readings are sent to the Arduino Mega micro-controller (MCU) through an

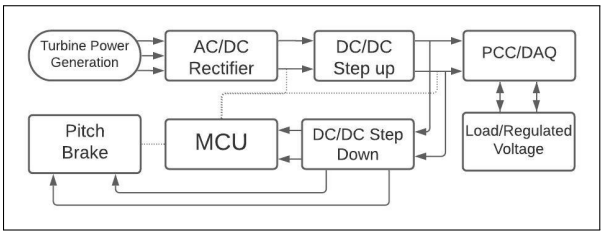

Fig. 23. Electric Topology

INA260 voltage sensor to be used in the control algorithm. This regulated voltage is then split into two separate circuits. The first is to the XL4015 DC/DC step down converter to power the MCU, the 28BYJ-48 stepper motor (pitching), and the PQ12-P linear actuator (braking). The second circuit leads to the point of common coupling (PCC) and load system developed by the group. Another INA260 power sensor is implemented prior to exiting the electrical housing to detect continuity between the turbine and PCC.

A. Component Analysis

The first step to the integration of the electrical and mechanical systems is the 3-phase generator. To perform efficiently at lower wind speeds, the group moved forward with an 110 kV generator. However, the lower kV rating resulted in lower FOS at higher rpm values. A runaway event at a wind speed of 22 m/s would result in a 72.7 V output from the turbine. This is not viable for any of the components implemented into the system, as seen in Table III. This table suggests a maximum value of 35 V.

TABLE III
Electrical Component Specifications

Component	Input	Output	Maximum
12 Ch. Slip Ring	-	-	10 A
18-Gauge Wiring	-	-	15 A
Rectifier	0-45 VAC	0-45 VDC	45 A
DC/DC Step Up	3-35 V	3-35 V	15 A
DC/DC Step Down	8-36 V	1.25-32 V	5 A
Voltage Sensor	0-36V	0-36V	15A
Load (0-4.75) Ω	-		100 W

This voltage production would be seen at a runaway event as early as 10.4 m/s, but would never occur within normal operating conditions. Therefore, in order to assure the safety of the electrical components within the circuit, an over-voltage protection event that will trigger the braking system at any voltage read out above 30 V prior to the DC/DC step up converter will be employed. In theory, the disconnection of the load would park the turbine before this command. The 5 V clearance has been implemented to raise the FOS (1.17) as well as account for any inaccuracy or delay added by the voltage sensor/MCU. An

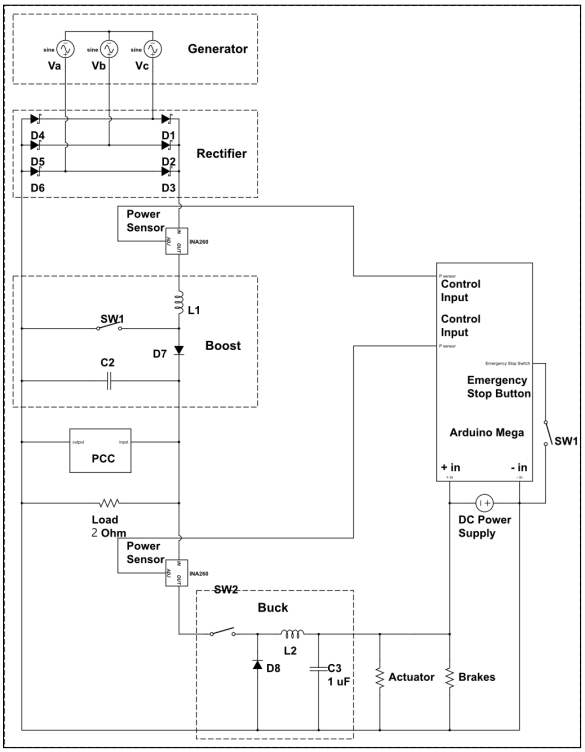

Fig. 24. Electric Diagram

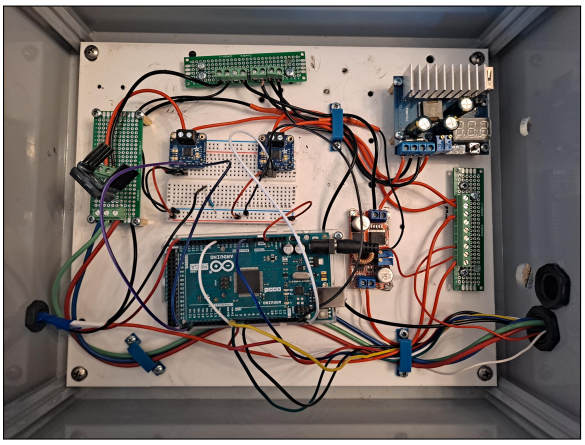

Fig. 25. Electrical Housing (Inner View)

electrical diagram of the components can be seen in Figure 24 along with the physical layout of the components seen in Figure 25.

Apart from the electrical housing, the NAU 2020 Energy Club fabricated a PCC for future CWC teams to use in testing. The team's PCC utilizes a LabVIEW UI and includes physical voltmeter and ammeters displays atop the housing to aid in troubleshooting. The PCC follows the connection methodology as described by the 2021 RR and has several extra ports for future teams to improve upon. One of the add-ons incorporated during the 2021 spring semester was a cup anemometer for wind speed readouts. Also included within the PCC black box is the emergency push button, which is another component that was handed down by previous NAU CWC teams.

The remaining electrical components of the system are the electrical loading and DC feedback. The loading should allow for optimum power output while ensuring current values below the maximums seen in Table III. With these considerations, a resistance of 2 Ω was selected. However, this is not the only safety concern associated with the loading. As testing is to occur within a vehicle, the group must safely secure the load within an enclosure so that no members or equipment are in danger when the turbine is in operation. The team utilized a metal enclosure handed down by previous NAU teams to ensure the safety of the involved individuals.

B. Control Logic

The turbine utilizes an Arduino Mega to control the turbine in operation. The algorithm will begin by checking the three shut down scenarios. The first is the over voltage protection event. If the voltage prior to the DC/DC step up is larger than 30 V, the turbine will pitch the blades to stall and then extend the actuator. However, because parking the turbine will reduce the voltage, the turbine would then inappropriately release the braking system in an over-speed event if the above condition was the only parameter for over-voltage protection. Therefore a manual aspect is introduced, where the emergency push button circuit must be opened and closed before operation is to resume. The same events will occur if the emergency button circuit has been opened (as per the RR) or the post DC/DC step up continuity returns an open circuit through the detection of voltage with no current. The algorithm will then loop itself until the emergency button is released and the load connection proves continuous, at which point the pitching loop will begin after releasing the braking system.

As mentioned in Section III, the variables that

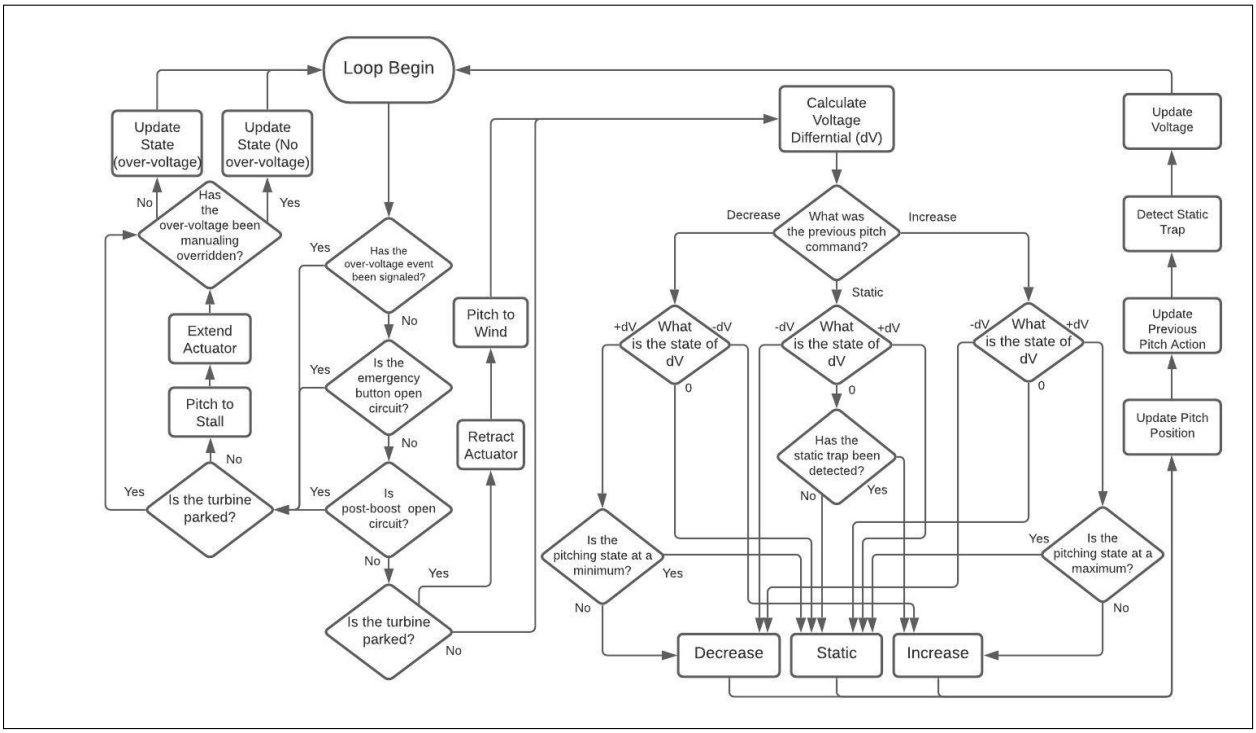

Fig. 26. Control Algorithm

determine the optimum pitch angle vary frequency and are challenging to accurately obtain in real time. In response to this, the group utilized a system that tracks the voltage differentials (dV) and compares them to the previous pitching action to determine the next appropriate command. For example, if the previous action pitched the blades closer to operating from a start up position (increase) and the voltage mirrored this magnification, it will once again *increase* the pitch. In contrast, if that increase produced a negative dV, the controls would then pitch from operating back to start up (decrease). If the magnitude of dV is below the designated threshold, the turbine will remain static. This logic is visualized in Figure 26.

There are several considerations that go into this logic that will optimize its performance and prevent it from malfunctioning. One of these considerations is the magnitude at which dV is considered non-zero. This value must be complimented by the incorporated delay as well as the increments at which the pitch is changed. Misalignment of these values can either result in a turbine that does not pitch and sits idol or one that is constantly pitching and drawing a needless amount of current. The team sets these values as 0.2 V with a 0.5 second delay in which the motor will pitch 1° ($\approx$ 6 steps). However, if the above logic was the extent of the algorithm, the unpredictable conditions of the wind could trap the turbine in a futile loop.

Assuming start-up position at the time of commissioning, the pitch position is tracked to avoid this. This allows the algorithm to prevent movement beyond the physically available pitching range. The final consideration is the static loop, where steady flow could result in the turbine remaining at sub-optimum pitch conditions. A tracking variable that persists for a number of loops will break this cycle if it is detected that the turbine has remained static with no voltage differential for too long. Although this has the potential to disrupt operating conditions, the algorithm will quickly return the turbine to ideal pitch positioning in that scenario.

IX. Design Overview

In the preceding sections, sub-systems have been individualistically discussed to justify the utilized

designs. This section will present the turbine in a comprehensive manner. This will be done through the visualization of the fabricated product as well as its accompanying testing apparatus. This is followed by an assessment of the turbine's conformity to the constraints established in Section II through the technical inspection checklist presented in Appendix B of the 2021 RR. This checklist will be shown in tandem with a summation of other safety measures mentioned throughout the document. The section will be concluded with the instructions for the turbine's commissioning.

A. Existing Prototype and Testing Apparatus

The blades, as well as their connection to the hub, are displayed in Figure 27. Following this, the pitching system is shown in Figure 28. The brake and generator mounting system (a sub-function of the upper nacelle) are highlighted in Figure 29. The yawing fin is displayed by a side view of the upper portion of the assembly in Figure 30. This figure also features the cover, which has been left out of other images for clear visibility. Figure 31 shows the management of wiring within the nacelle, as well as a portion of the nacelle-tower connection. Figure 32 displays not only the weldment and M10 clearence holes of the baseplate, but also depicts the apparatus used to prevent the crushing of wires when not in commission.

Accompanying the physical turbine are the electrical systems. The team's electrical housing, which contains all components listed in Table III other than the slip ring and variable load, is seen in Figure 33. Next is the Energy Club's PCC and resistive load, present in Figures 34 and 35. Note that the enclosure shown would have the lid bolted over the load when in commission. Finally, the group utilizes a Jeep Wrangler (Figure 36) with a detachable roof to attach a plywood apparatus atop the vehicle to test the turbine, the installation of which is precisely documented in the commissioning subsection to follow.

B. Design Inspection

The team's principal investigator acted as the judge for the unofficial technical inspection. All safety requirements have been met and most non-safety requirements have been either met or addressed.

Fig. 27. Rotor

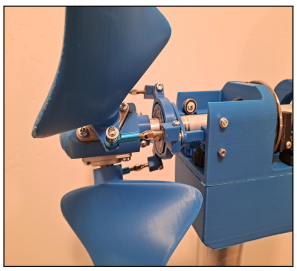

Fig. 28. Pitching System

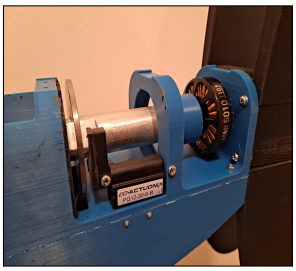

Fig. 29. Brake System

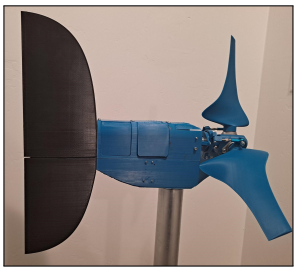

Fig. 30. Yaw Fin

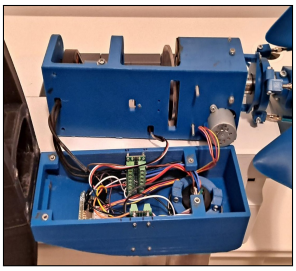

Fig. 31. Lower Nacelle

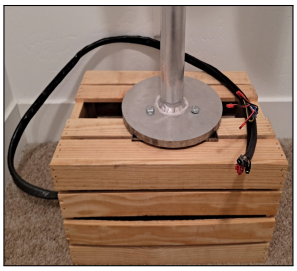

Fig. 32. Base Plate

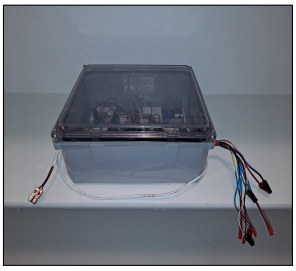

Fig. 33. Electrical Housing

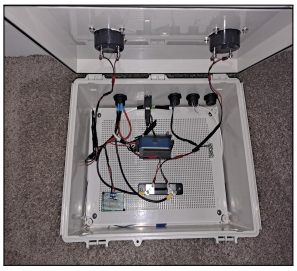

Fig. 34. In-House PCC

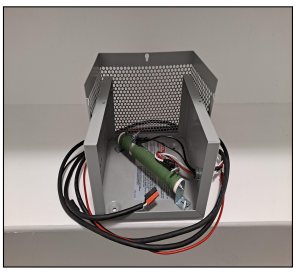

Fig. 35. Resistive Load

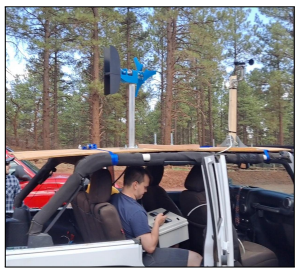

Fig. 36. Testing Apparatus

The following enumeration represents the only categories where the team's design strayed from regulation.

- The turbine mid-plane sits at 710 mm.
- The base plate diameter at 228 mm (9").

These anomalies are the result of prioritizing interfacing with the in-house apparatus. The rotor mid-plane sits at 710 mm from the base plate's bottom. This was done to retain the same height as the preexisting NAU Energy Club's anemometer equipment. Furthermore, the base plate's diameter was left at a larger diameter of 22.8 cm (9") to ensure a safer connection to the plywood apparatus.

Even beyond the official measures, the design of machines rotating at thousands of rpm need a considerable number of safety precautions. Parts discussed throughout the document have received both analytical and experimental verification of their performance under their most strenuous operating conditions. Those efforts are summarized in Table IV. Up until this point, presented FOS have only considered worst-case scenarios. For comprehensive documentation of the turbine, Table IV includes values for other relevant states of the turbine using the same analyses previously implemented. This includes situations that would theoretically not occur under the management of the control system. The team thought it valuable to understand where the turbine would fail even outside of designed operation. The only scenarios that are forgone are those where runaway conditions at 22 m/s still result in FOS above 10 (i.e. the shaft).

The final topics to address in this inspection are the designs inspired by previous CWC participants, both within and outside the confines of NAU. All inspired designs have been addressed in their respective sections, but the summation of these inspirations can be seen in Table V.

TABLE IV
MINIMUM FACTORS OF SAFETY

Part	Conditions	FOS
Blade	Runaway (22 m/s)	1.17
	Runaway (13 m/s)	3.67
	Operating (13 m/s)	15.87
	Operating (11 m/s)	21.47
	Voltage Protection	7.77
Hub	Runaway (22 m/s)	0.54
	Runaway (13 m/s)	1.63
	Operating (13 m/s)	6.58
	Operating (11 m/s)	9.16
	Voltage Protection	3.11
Brake	Operating (22 m/s)	5.31
	No stall (22 m/s)	2.32
	Operating (13 m/s)	14.38
	No stall (13 m/s)	6.60
Shaft	Runaway (22 m/s)	183.6
Base-plate	Operating (22 m/s)	24.5
Tower-Nacelle Connection	Operating (22 m/s)	11.4
Electronics	Runaway (22 m/s)	0.47
	Runaway (13 m/s)	0.80
	Operating (13 m/s)	1.72
	Operating (11 m/s)	2.03
	Voltage Protection	1.17

TABLE V
INSPIRED DESIGNS

Inspiration	Design Description
2020 NAU	Pitching that utilizes a swash plate
2020 NAU	Load safety enclosure
2020 NAU	Emergency stop button
2019 PSU	NACA0009 profile for fin wings
2018 NAU	Rubber backing for brake disk

C. Commissioning

When installing the turbine in the field, there are several considerations that need to be made. These considerations are not only for the safety of the students operating the machinery, but also for the ideal operation of the turbine.

Prior to moving the turbine, confirm that...

- the base-plate is mounted to the wooden support and all wiring is fed through the clearance hole so that no wires are crushed under the weight of the apparatus.
- the blades are pitched to stall so that any ambient wind will not cause rotation that could injure on-site technicians.
- all Anderson and/or JST interconnections between the turbine, electrical box, PCC, load, and power supply are disconnected.

While moving the turbine, be sure that...

- two people accompany the turbine at all times. One to support the weight of the turbine and maneuver through enclosures, another to open doors, keep the wiring from touching the ground, and aid the individual carrying the turbine in any manner required.
- other components can be moved by a single individual, but efforts should be made that no wiring is dragging behind the individual that could get caught on doors, furniture, etc.

The following instructions are specific to the team's testing apparatus that was previously displayed in Figure 36, but similar guidelines should be followed in any testing or operating environment. When installing the turbine...

- remove the roof of the testing vehicle. This should be done without any turbine components in the nearby vicinity.
- place the plywood frame atop the roofless vehicle and insert the 2"x4" anchor along the plywood over the center bolt holes.
- with one member within the vehicle and another accessing the top, feed the two M12 bolts through the clearance in the car's overhead frame, at which point the locking nuts can be wrenched down to the 2"x4" anchor.
- using ratchet straps, secure the plywood to the front and back of the vehicle. This should involve an extra wrap around any available sections of the vehicle frame.
- the anemometer can now be installed at any of the plywood corners. From within the vehicle, feed four M10 bolts through the plywood so an individual above the vehicle can secure them with locking nuts.
- the installation of the turbine should involve three individuals, one within the vehicle and two others outside supporting the weight of the turbine. Feed the cabling through the center clearance and align the 3 M10 bolt holes. Using M10 bolts, torque down the turbine with wing nuts to 50 N·m (If tooling is available).
- Prior to securing the final wing nut, insert the 12 mm ring terminal around the bolt. This is attached to an 18-gauge wire that acts as a tower ground and is fed directly into a JST outside the electrical box. There is a separate clearance for this wire in the plywood 5 cm outside the perimeter of the base-plate.
- Place all other components (electrical box, PCC, load, and power supply) within the vehicle and make all necessary connections. The turbine to electrical interface has 5 Anderson connections (3-Phase and 6V feedback) along with 6 JST connections (stepper control, actuator control, and tower ground). All are clearly labeled at each side of the connection.
- the electrical box to PCC to load connections all feature clearly labeled Anderson connections. The only remaining wiring is the parallel connection of the power supply to the load, which is done through typical color coded DC power supply headers. To power the supply within the vehicle, a 12 VDC to 120VAC inverter is required.
- once all components are secure within the vehicle and the blades have been repositioned to start up, the turbine is ready for operation. Be sure that the PCC is easily accessible so power production can be monitored and the emergency stop button is readily available.

X. Dynamic Testing

In midst of the global pandemic where access to wind tunnels is scarce, the team utilized a group member's personal vehicle to simulate a flow field as previously shown in Section IX. Figure 37 shows this vehicle on a secluded forest service road with the turbine in operation.

Fig. 37. Dynamic Vehicle Testing

A. *Vehicle Testing*

The group was capable of testing start up, operating, and parked conditions. The results of these tests are shown in Figure 38. Examining the raw data, parked conditions displayed promising results, keeping the turbine static at wind speeds up to 13 m/s with no significant power production. The trends in the other testing scenarios indicate issues with start up and power output at winds speeds at and above the rated regime despite the visually apparent rotational velocity obtained. The maximum power achieved was 11.14 W at a wind speed of 21.5 m/s. At this particular instance, the achieved voltage was 5.84 V. This explains why the control algorithm did not shut down the turbine, as substantial voltage losses were experienced and the system did not approach the over-voltage protection event despite the higher wind speeds.

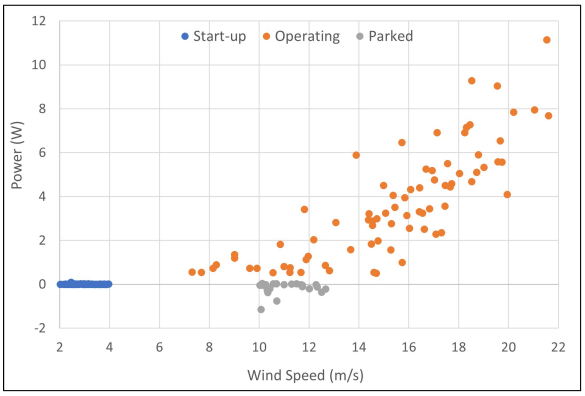

Fig. 38. Dynamic Testing Results

B. *Electrical Investigations*

This level of power production is an order of magnitude lower than Q-Blade estimations (425 W at 21.5 m/s). This drastic difference was a strong indication of a malfunctioning electrical component. In order to address some of the problems seen, the group re-examined the electronics in a comprehensive manner. The testing apparatus is seen in Figure 39. Once a steady rotational velocity was obtained by the dynamo-meter, the line to line 3-phase, pre-step up, and post-step up voltages were all read in tandem with the output of the PCC. Although the dynamo-meter was in use, the generator supplied power through the same configuration shown in Figure 31 with one extra terminal prior to the headers located in the lower nacelle.

Fig. 39. Electrical Testing Apparatus

It was discovered that the generator was out of phase and the line to line voltages were varying up to 1.5 V. After several tests were run consisting of three different generators of different kV rating and multiple electrical configurations to troubleshoot the experienced issues, the group theorized the problem was a faulty rectifier. After replacing the component, the group ran a full electrical system test that resulted the values present in Figure 40. The values obtained through testing are compared to the maximum power output that could be seen at that rotational velocity as derived by Q-Blade. This data shows a more appropriate capacity that will result in more appropriate power production in future vehicle tests.

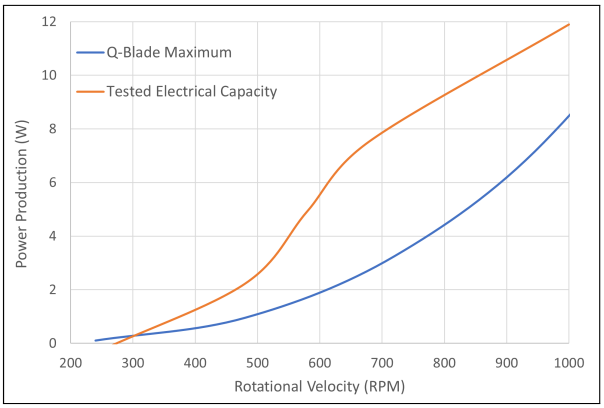

Fig. 40. Tested Electrical Capacity

XI. Conclusions

NAU's 2021 CWC turbine team has produced a mechanically and electrically functioning turbine

as per the regulations set forth by the DOE in the RR. The blades produced have a theoretical efficiency over 45% and have been tested and simulated to confirm the structural capability of the blade to withstand a variety of scenarios including rotational velocities up to 8000 rpm. A unique pitching system was then developed to increase the performance of the blades in a variety of scenarios, producing nearly 0.02 N·m of torque at wind speeds as low as 3 m/s and reducing torque down to 0.65 N·m in strenuous flow regimes (22 m/s). Other critical subsystems include the brake and yaw. The braking mechanism boasts a FOS of 5.31 after many safety precautions employed in the initial designs. The yaw system proved efficient in live testing in a variety of wind speeds with no signs of structural damage. These physical designs were then complimented by electrical systems and control algorithms that were carefully adjusted to withstand the expected scenarios and optimize the operation of the turbine. Live vehicle testing then highlighted ways to prevent power loss, which was then confirmed through the comprehensive testing of the electrical system in a controlled environment. The product seen documented throughout the report is not only a result of the efforts put forward by the group members, but also of the support the group received financially, academically, and emotionally from NAU faculty, DOE representatives, and the community developed by the CWC and the wind industry in Flagstaff and throughout the United States. The group looks forward to involving themselves with NAU's 2022 CWC team and act as that support as more young engineers explore the physics and design considerations that are embedded within the study and research of wind turbines.

REFERENCES

[1] U. D. of Energy, "Cwc2021 rules and requirements," 2021.

[2] J. F. Manwell, J. G. McGowan, and A. L. Rogers, *Wind energy explained: theory, design and application*. John Wiley & Sons, 2010.

[3] W. Shuhua, X. Qiaoli, L. Fen, D. Jinming, H. Jia, and X. Bingshe, "Preparation and properties of cellulose-based carbon microsphere/poly(lactic acid) composites," *Journal of Composite Materials*, vol. 48, 04 2014.

[4] L. Duncan *et al.*, "CWC20 NAU Technical Design Report," *United States Department of Energy*, 2020.

[5] M. Cruz Gómez, E. Gallardo-Hernández, M. Vite Torres, and A. Peña Bautista, "Rubber steel friction in contaminated contacts," *Wear*, vol. 302, no. 1, pp. 1421–1425, 2013, wear of Materials 2013. [Online]. Available: https://www.sciencedirect.com/science/article/pii/S0043164813001099

[6] A. Proulx, S. Rich, J. Kaewvichien *et al.*, "The Pennsylvania State University Wind Energy Club Technical Design Report," *United States Department of Energy*, 2019.

[7] B. Liu, R. Villavicencio, and C. Guedes Soares, "Failure characteristics of strength-equivalent aluminium and steel plates in impact conditions," 03 2013.